Supporting information

Understanding the thermally activated charge transport in $NaPb_mSbQ_{m+2}$ (Q = S, Se, Te) thermoelectrics: weak dielectric screening leads to grain boundary dominated charge carrier scattering

Tyler J. Slade,[1] Jann A. Grovogui,[2] Jimmy Jiahong Kuo,[2] Shashwat Anad,[2] Trevor P. Bailey,[3] Maxwell Wood,[2] Ctirad Uher[3], G. Jeffrey Snyder,[2] Vinayak P. Dravid,[2] Mercouri G. Kanatzidis[1]

[1]Department of Chemistry, Northwestern University, Evanston, Illinois 60208, USA.
[2]Department of Materials Science and Engineering, Northwestern University, Evanston, Illinois 60208, USA.
[3]Department of Physics, University of Michigan, Ann Arbor, Michigan 48109, USA.

Corresponding author: M. G. Kanatzidis (m-kanatzidis@northwestern.edu).

Additional discussion of the GB scattering model presented in the main text:

In the main text, we estimated the grain boundary (GB) energy barriers in our $NaPb_mSbQ_{m+2}$ materials by using a model that was original derived by Seto to account for electrically resistive GBs in polycrystalline silicon films. This earlier paper found two expressions for the barrier height at the GBs, each of which depends on the doping level as follows:[1]

$$E_b = \frac{e^2 L^2 N}{8\varepsilon} \quad \text{if } LN < Q_t \tag{S1}$$

$$E_b = \frac{e^2 Q_t^2}{8N\varepsilon} \quad \text{if } LN > Q_t \tag{S2}$$

Where L is the grain size, N the doping density, Q_t the concentration of trap states at the GBs, and ε the dielectric constant. Equation S1 corresponds to a situation where the charge carrier density is smaller than the density of trap states and Equation S2 to the carrier density greater than Q_t. We believe Equation 2 is more applicable to our samples for the following reasons. Both Figure 2 in the main text and Figure S5 show that at temperatures greater than 500 K, the electrical conductivities of the small grained SPS processed samples converge to the values measured for the large grained slow cooled ingots. This indicates that the bulk conductivity is largely unaffected by the presence of the GB trap states. In the case of Equation S1, the grains would be completely depleted of charge carriers,[1] and if this were the case, the bulk conductivity should be characteristic of an undoped semiconductor. On the contrary, Figures 2 and S5 both indicate that the bulk conductivities are characteristic of degenerate doping. Moreover, Equation 1 predicts that the energy barriers will be greater for larger grained samples, which is also contrary to our experimental observations, as the data in Figure 2 and S5 show the GB scattering is eliminated in the larger grained samples. Based on these factors, we believe Equation 2 is more applicable to our $NaPb_mSbQ_{m+2}$ materials. Ultimately, because both equations are inversely proportional to ε, this choice does not substantially impact the arguments discussed in the main text.

Figure 4 in the main text provides evidence that the GB charge carrier scattering is strongest in more ionic $NaSbSe_2$-rich phases of the PbSe-$NaSbSe_2$ system. Moreover, Figure 5 shows that GB scattering is stronger in the most ionic PbS-$NaSbS_2$ family. This analysis provides solid support for our central hypothesis, suggesting that weakly polarizable materials composed of small and ionic atoms will be more prone to GB charge carrier scattering than highly polarizable compounds like PbTe. To support the data present in the main text, we note that Figure 4

demonstrates that at high temperatures, the electrical conductivities are lowest for the $NaSbSe_2$ rich phases, indicating that the bulk conductivities (σ_G) decrease with greater $NaSbSe_2$ fraction. This is reasonable, because our earlier work demonstrated that addition of $NaSbSe_2$ to PbSe increases the charge carrier effective mass and thus lowers the carrier mobilities.[2] The different bulk electrical conductivities are however potentially important, as Equation 3 indicates that reliably analyzing the GB contribution to the electrical conductivity requires $\sigma_G >> \sigma_{GB}$, which occurs when σ_G is very high and/or when E_b is also large. The different bulk conductivities of the samples discussed above thus could in principle obscure our analysis. Therefore, to supplement the data found in Figure 4 and provide another measure of the GB contribution at different $NaSbSe_2$ fractions, we compared three additional samples (again m = 20, 10, 6) that have similar bulk electrical conductivities. The data is presented in Figure S10. The electrical conductivities of each sample converge above ~600 K, suggest similar values of σ_G. The energy barriers again increase with $NaSbSe_2$ fraction, with estimated values of 19 and 68 meV for m = 10 and 6 samples respectively. The GB scattering in the m = 20 sample was too weak to extract a barrier height, suggesting a very small E_b, consistent with our findings in Figure 4. These findings provide greater support for our hypothesis, indicating substantially larger values of E_b for ionic $NaSbQ_2$ rich phases.

The Seebeck coefficients indicate negligible ionized impurity scattering:

The electrical properties discussed in the main text for large and small grain samples provide firm and unambiguous evidence linking the low temperature charge carrier scattering to the GBs. The large and small grained samples we compare have negligible differences in chemical composition, meaning that impurity scattering in each will be the same. Therefore, we can directly attribute the low temperature scattering found in small grain samples, but not in large grained samples, to the grain size.

We can even more conclusively rule out ionized impurity scattering by considering the temperature dependence of the Seebeck coefficients. While impurity scattering can in principle give a similar temperature dependence for the electrical conductivity and charge carrier mobility, we believe that ionized impurity scattering is insufficient to explain the experimental Seebeck coefficients. This can be easily seen by the equation for the Seebeck coefficient in a single parabolic band model

$$S = \frac{k_B}{e}\left(\frac{(r+5/2)F_{r+3/2}(\eta)}{(r+3/2)F_{r+1/2}(\eta)} - \eta\right) \quad (3)$$

where k_B is the Boltzmann constant, η is the reduced chemical potential, $F_r(\eta)$ are the Fermi-Dirac integrals, and r gives the energy dependence of the carrier relaxation time. In the cases of acoustic phonon and ionized impurity carrier scattering, r is equal to -1/2 and 3/2 respectively. In the above equation, the temperature dependence of the Seebeck coefficients is contained in the $F_r(\eta)$ terms, showing that if the low T scattering is due to ionized impurity scattering, r would switch from 3/2 to -1/2 near ~500 K when acoustic phonon scattering begins to dominate the transport. Such a change in r should alter the temperature dependence of the Seebeck coefficients, which is clearly not observed in our experimental data, indicating ionized impurity scattering is negligible in our samples.

Explanation of the contradictory trends in lattice thermal conductivity:

The estimated lattice thermal conductivities shown in Figures S12 and S13 show an apparent contradictory trend, appearing to be largest in the small grained samples with strongest GB scattering. This issue was also pointed out in our previous work[2] and is an artifact stemming from improper estimation of κ_{elec} that occurs when GB scattering is dominant. We give a detailed account of this anomalous behavior elsewhere,[3] which we briefly explain here as follows:

The lattice thermal conductivity κ_{lat} is estimated by subtracting the electronic thermal conductivity κ_{elec} from the total thermal conductivity κ_{tot}, and the electronic contribution is estimated using the Wiedemann-Franz law, giving $\kappa_{lat} = \kappa_{tot} - \sigma LT$, where σ is the electrical conductivity, L is the Lorenz number, and T is the temperature. In a material with GB scattering, the electrical conductivity is given by $\sigma^{-1} = (1-t)\,\sigma^{-1}_G + t\,\sigma^{-1}_{GB}$ (Equation 3 in the main text), where t is the GB thickness, σ_G is the conductivity in the bulk grains, and σ_{GB} is the conductivity across the GBs. When GB scattering is strong, i.e. $\sigma_G >> \sigma_{GB}$, the total electrical conductivity is approximately $\sigma \approx \sigma_{GB}$. In this situation, the Wiedemann-Franz law to estimate the lattice thermal conductivity becomes $\kappa_{lat} = \kappa_{tot} - \sigma_{GB}LT$. Unfortunately, *this expression completely neglects that charge carriers still transport heat through the bulk grains*. At the boundary, the thermal transport

across the GBs can switch from the high resistance electrical channel to the lower resistance phonon transport channel. In this context, the correct form of the Wiedemann-Franz law for thermoelectric materials with electrically resistive GBs is $\kappa_{elec} = \sigma_G LT$. Using this relationship accounts for heat transported by carriers through the grains and thus allows for correct estimation of the true lattice thermal conductivity and eliminates the apparent contradiction observed between grain size and lattice thermal conductivity. Because the present work focuses on understanding of the electrical properties, this is ultimately outside the scope of this paper.

Additional data:

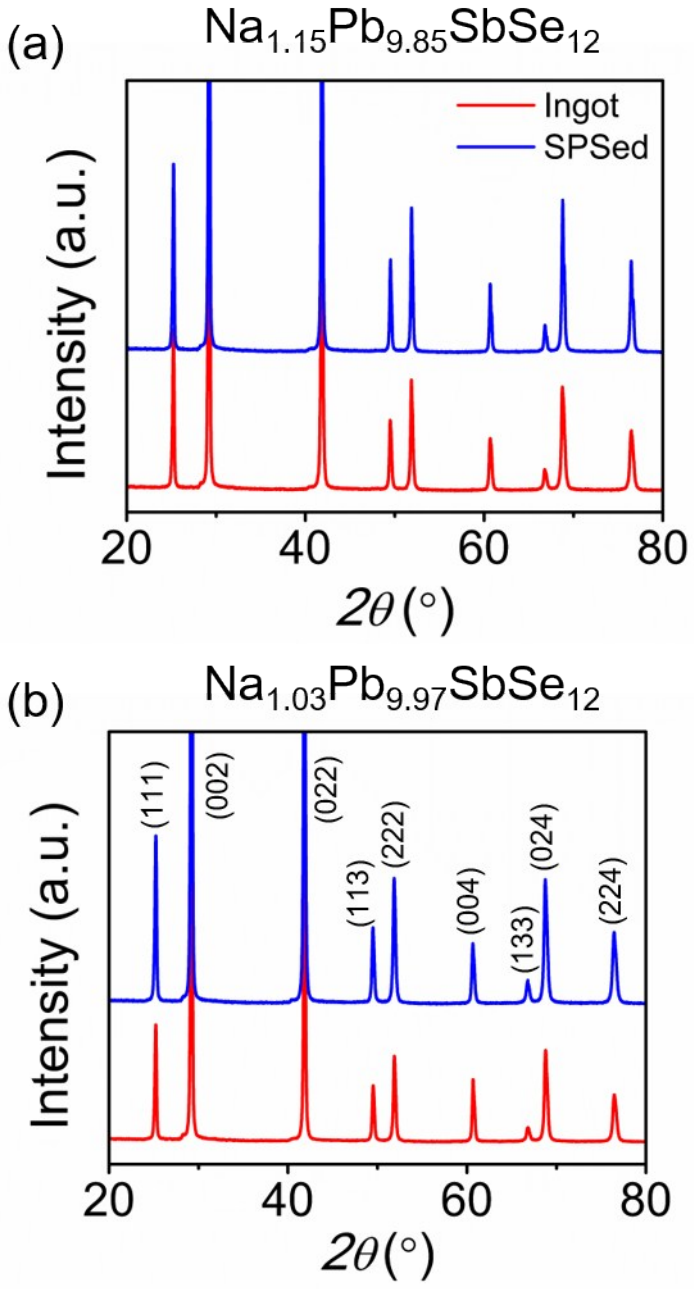

Figure S1: Comparison of the powder X-ray diffraction patterns of SPS-processed and as-cast ingots of p-type doped $Na_{1+x}Pb_{10-x}SbSe_{12}$. (a) is for x = 0.15 and (b) for x = 0.03. In both cases, the PXRD patterns show the expected peaks characteristic of the rocksalt structure with no evidence for secondary phases. These patterns suggest negligible chemical changes between SPS-processed and ingot forms.

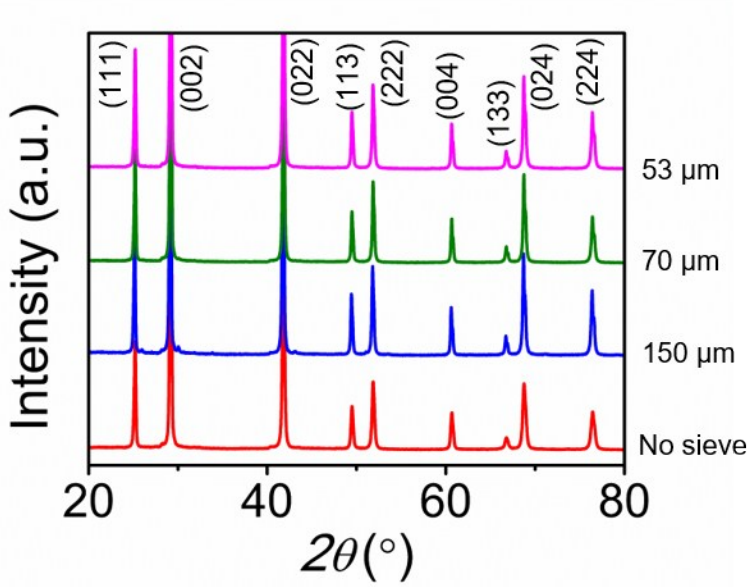

Figure S2: Powder X-ray diffraction patterns of SPS-processed samples prepared with different mesh sieves. All samples have the same nominal composition $Na_{1.10}Pb_{9.90}Sb_{0.90}Se_{12}$. The diffraction patterns all suggest each is a phase pure material with negligible chemical differences.

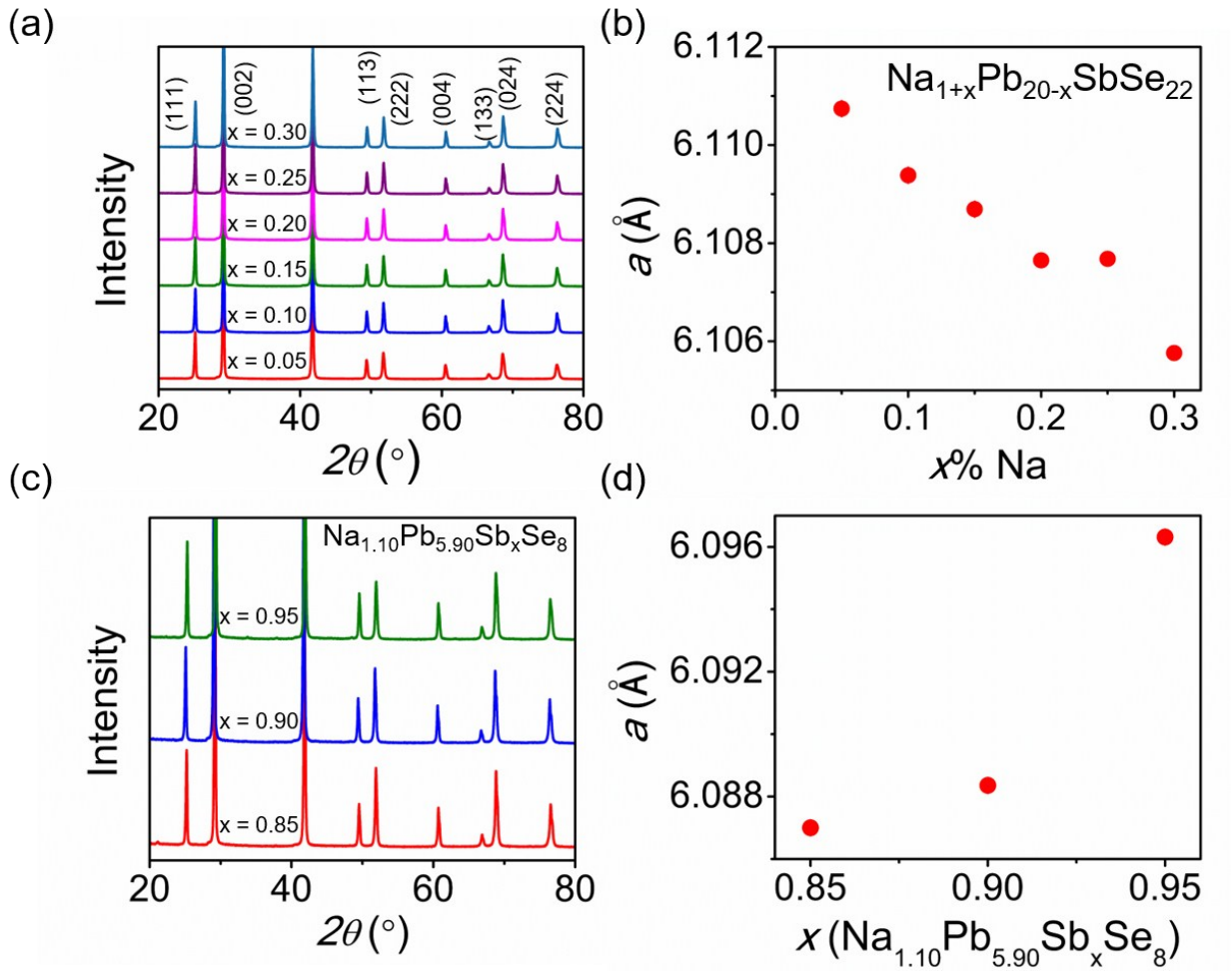

Figure S3: Powder X-ray diffraction patterns for p-type doped $NaPb_mSbSe_{m+2}$ for m = 20 and m = 6 (equivalently ~ 4% and 14% $NaSbSe_2$ in PbSe respectively). Nominal compositions are $Na_{1+x}Pb_{20-x}SbSe_{22}$ and $Na_{1.10}Pb_{5.90}Sb_xSe_8$. (a) and (c) are the PXRD patterns, and (b) and (d) are the respective lattice parameters. In general, all patterns show the expected peaks characteristic of the rocksalt structure and the lattice parameters change (approximately) linearly with doping, indicating successful Na incorporation. A very small amount of secondary phase is found for the pattern for m = 6, x = 0.95 in (c).

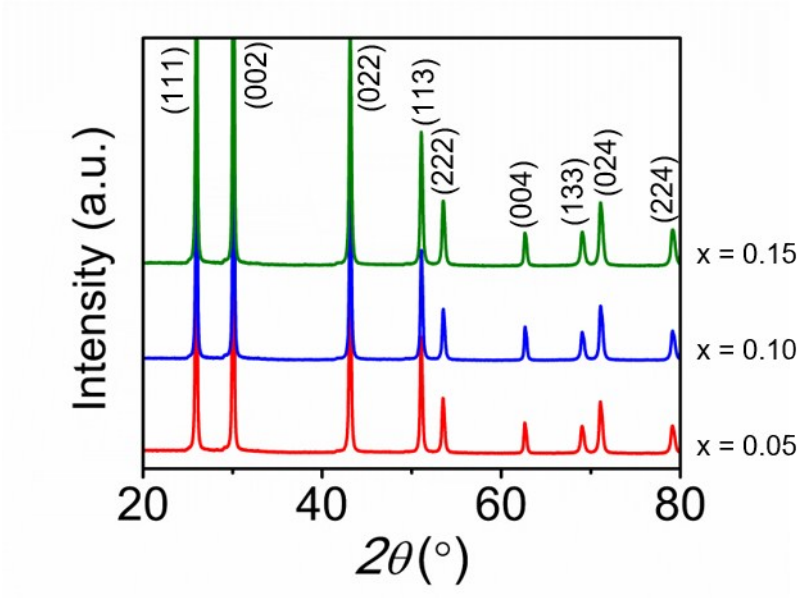

Figure S4: Powder X-ray diffraction patterns for p-type doped $Na_{1+x}Pb_{20-x}SbS_{22}$ (m = 20, equivalently ~4% $NaSbS_2$). The powder patterns show only peaks corresponding to the expected rocksalt reflections. No reflections corresponding to secondary phases are observed.

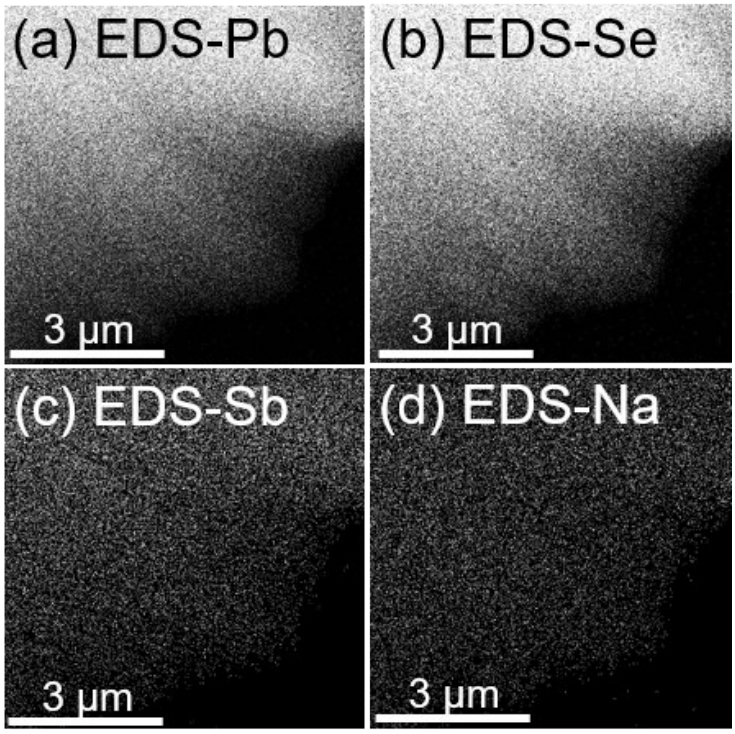

Figure S5: EDS maps over the GB region of the $Na_{1.15}Pb_{9.85}SbSe_{12}$ sample whose TEM and STEM images are discussed in Figure 3 of the main text. The EDS maps also show a homogeneous distribution of elements supporting that there is negligible phase or dopant segregation at the GBs.

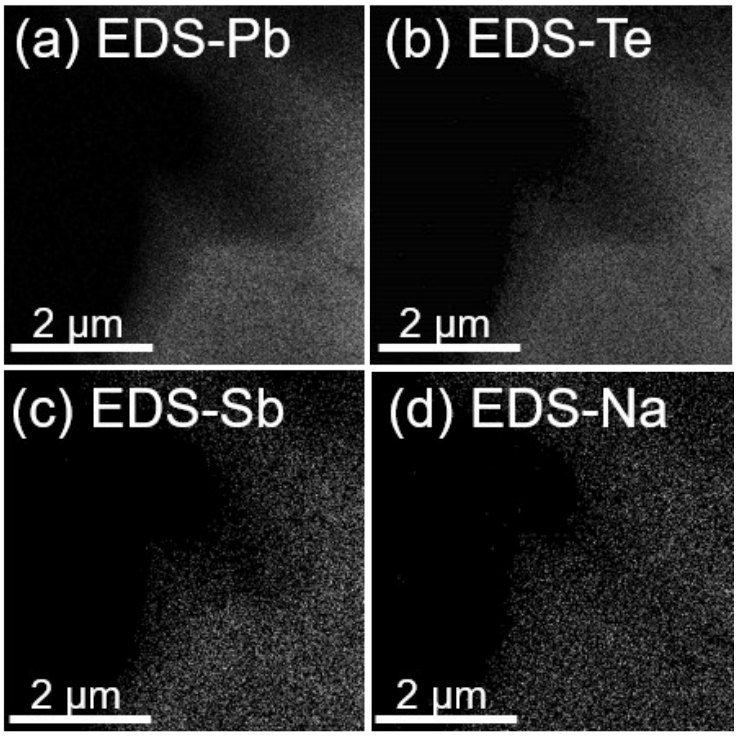

Figure S6: EDS maps over the GB region of a telluride sample with nominal composition $Na_{1.15}Pb_{9.85}Sb_{0.85}Te_{12}$ whose TEM and STEM images are discussed in Figure 3 of the main text. The EDS maps also show a homogeneous distribution of elements supporting that there is negligible phase or dopant segregation at the GBs.

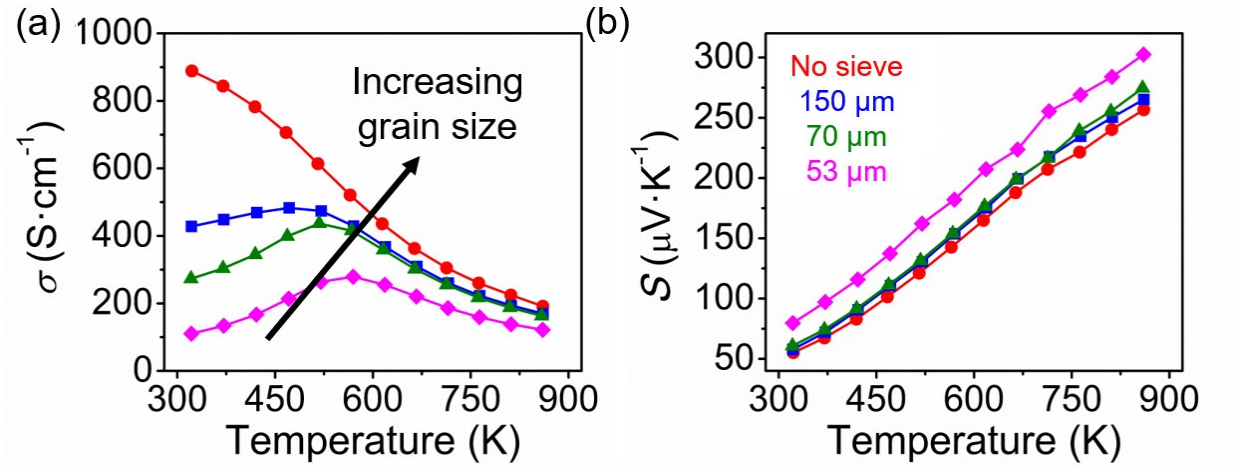

Figure S7: Electrical and thermal transport properties of samples with nominal composition of $Na_{1.10}Pb_{9.90}Sb_{0.90}Se_{12}$ prepared to have different sized grains by passing powdered ingots through different mesh sieves. (a) Electrical conductivities, (b) Seebeck coefficients. The sample passed through a 53 μm sieve likely has a somewhat smaller charge carrier concentration than the other samples, as evidenced by the greater Seebeck coefficient over the full temperature range.

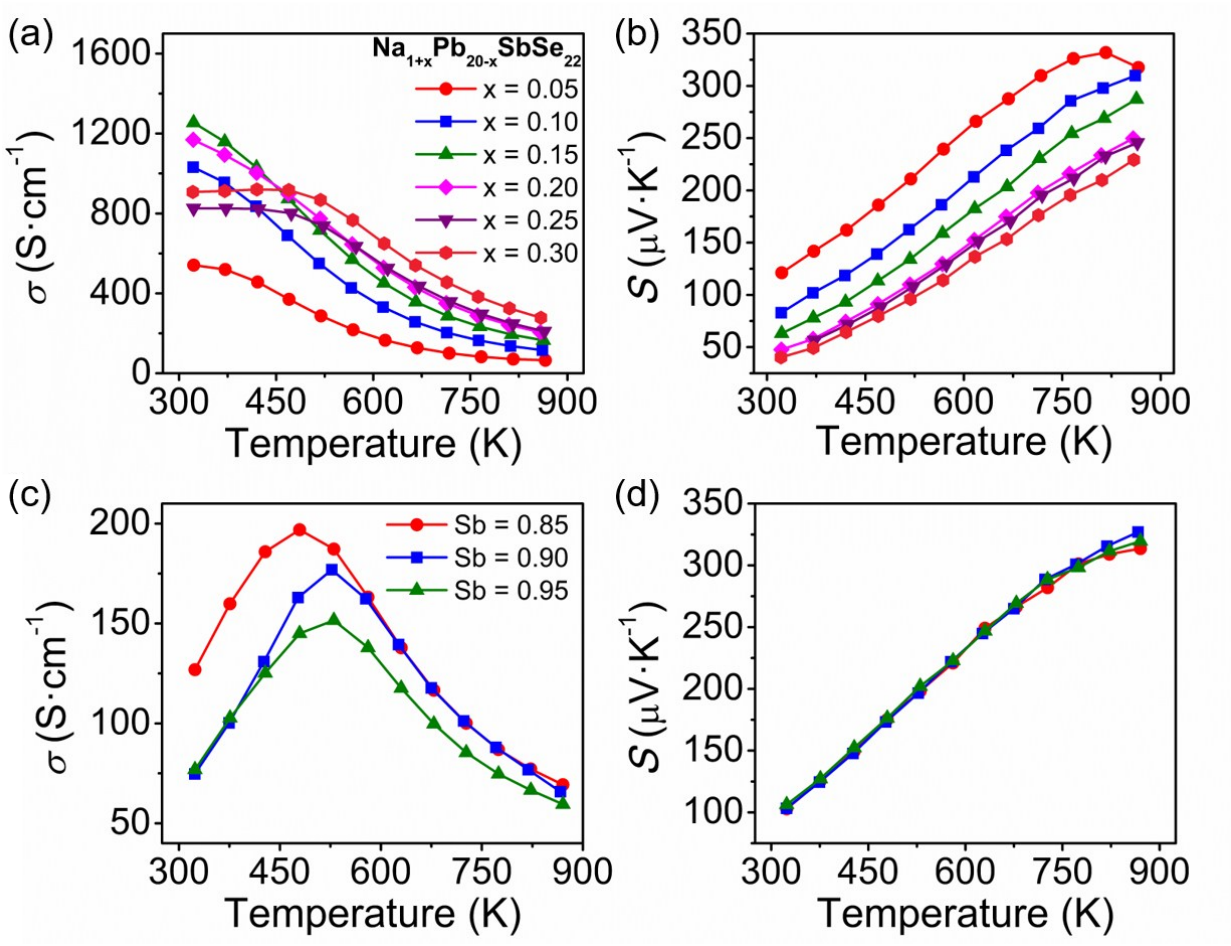

Figure S8: Comparison of the electrical properties for p-type doped $NaPb_mSbSe_{m+2}$ for m = 20 and m = 6 (equivalently ~ 4% and 14% $NaSbSe_2$ in PbSe respectively). Nominal compositions are $Na_{1+x}Pb_{20-x}SbSe_{22}$ and $Na_{1.10}Pb_{5.90}Sb_xSe_8$. (a) Electrical conductivities and (b) Seebeck coefficients for the m = 20 compounds. (c) Electrical conductivities and (d) Seebeck coefficients for the m = 6 phases. Clearly, comparing (a) and (c) shows that the m = 6 compounds have qualitatively stronger GB scattering, manifesting in a greater degree of suppression of σ under ~ 600 K.

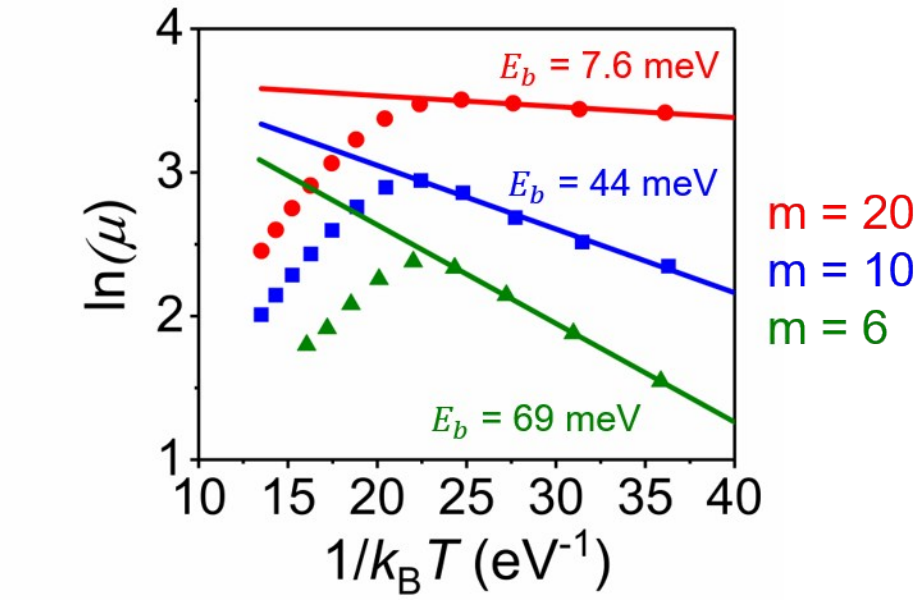

Figure S9: Plots of lnμ against 1/$k_B T$ for the m = 20, 10, and 6 $NaPb_mSbSe_{m+2}$ discussed in Figure 4 of the main text. The low temperature linear regimes are dominated by GB scattering, and the extracted energy barriers from the slopes agree well with the values estimated from the plots of lnσ vs 1/$k_B T$. Nominal compositions are as follows: $Na_{1.30}Pb_{19.70}SbSe_{22}$ (m = 20), $Na_{1.15}Pb_{9.85}SbSe_{12}$ (m = 10), and $Na_{1.10}Pb_{5.90}Sb_{0.90}Se_8$ (m = 6).

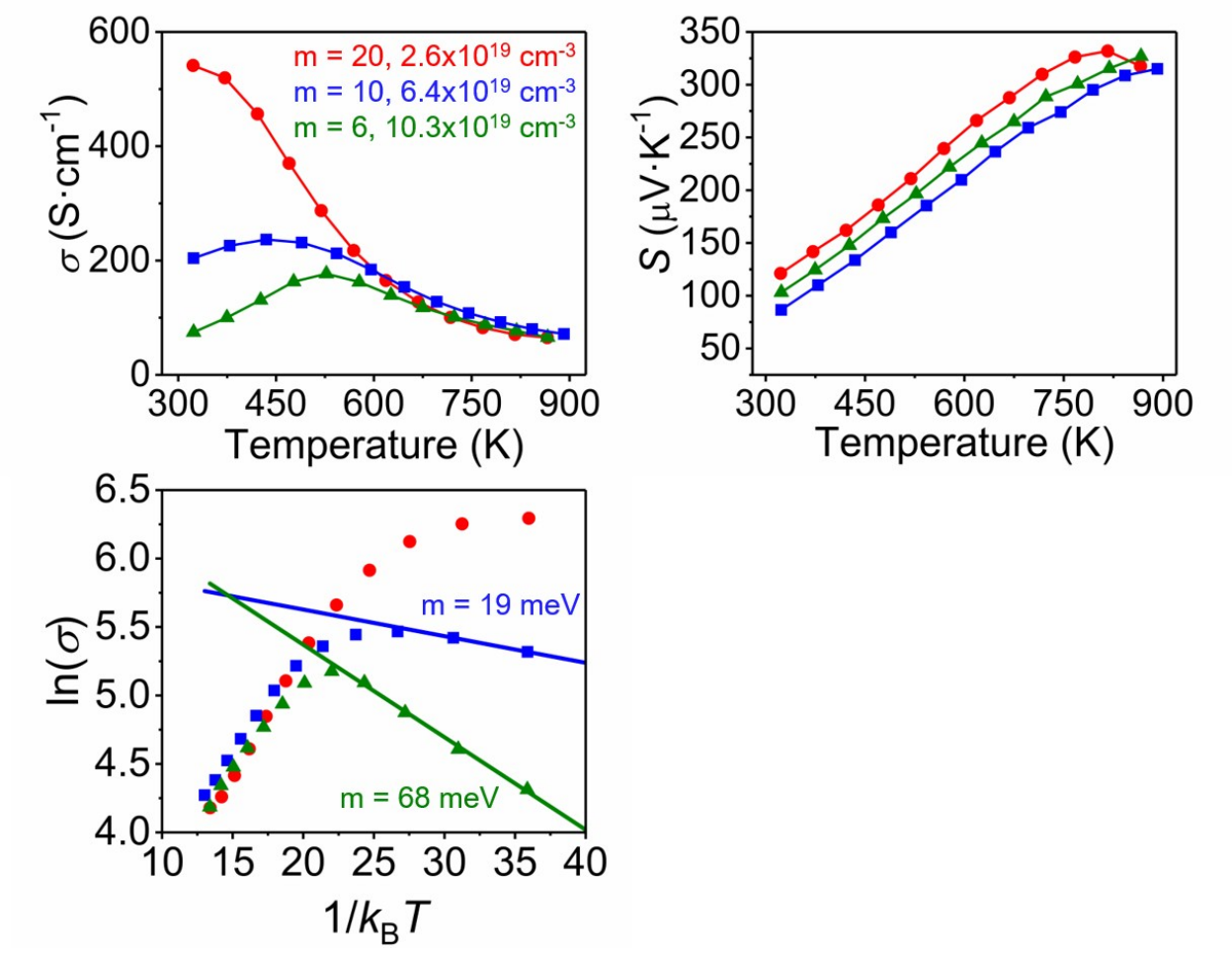

Figure S10: (a) Temperature-dependent electrical conductivities for three $NaPb_mSbSe_{m+2}$ (m = 20, 10, 6) samples that have similar bulk electrical conductivities σ_G. Because the high temperature conductivities converge, we believe σ_G is similar in each. The room-temperature charge carrier concentrations measured for each are given in the legend. Because the bulk charge carrier mobility decreases with $NaSbSe_2$ fraction (smaller m), the carrier concentrations are smallest in the high m samples to maintain comparable σ_G. (b) Temperature-dependent Seebeck coefficients for the same samples. (c) Plots of $\ln\sigma$ vs. $1/k_BT$ for each sample, showing that the barrier height increases with $NaSbSe_2$ amount, consistent with the data discussed in Figure 4 of the main text. Because the electrical conductivity in the m = 20 sample is not thermally activated and is only weakly suppressed near room temperature, we were unable to calculate a barrier height, suggesting a low E_b. Nominal compositions for each sample are as follows: $Na_{1.05}Pb_{19.95}SbSe_{22}$ (m = 20), $Na_{1.05}Pb_{9.95}SbSe_{12}$ (m = 10), and $Na_{1.10}Pb_{5.90}Sb_{0.90}Se_8$ (m = 6).

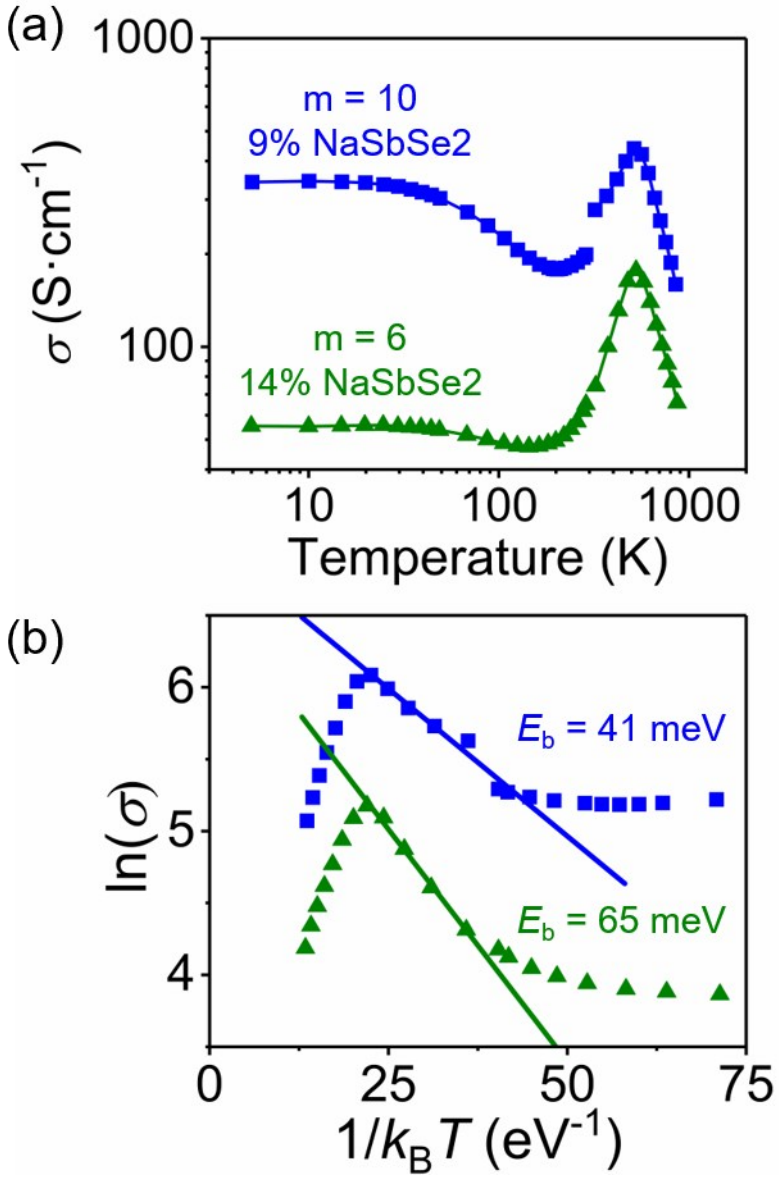

Figure S11: (a) Low–temperature electrical conductivities for m = 10 and 6 samples of $NaPb_mSbSe_{m+2}$ (respectively ~9 and 14 percent $NaSbSe_2$ in PbSe). The high–temperature data is also included and matches up well with the low–temperature results. (b) Plots of $\ln\sigma$ vs $1/k_BT$ including the low–temperature data from (a). The estimated energy barriers agree well with the results only considering the high–temperature data discussed in Figure 4 of the main text.

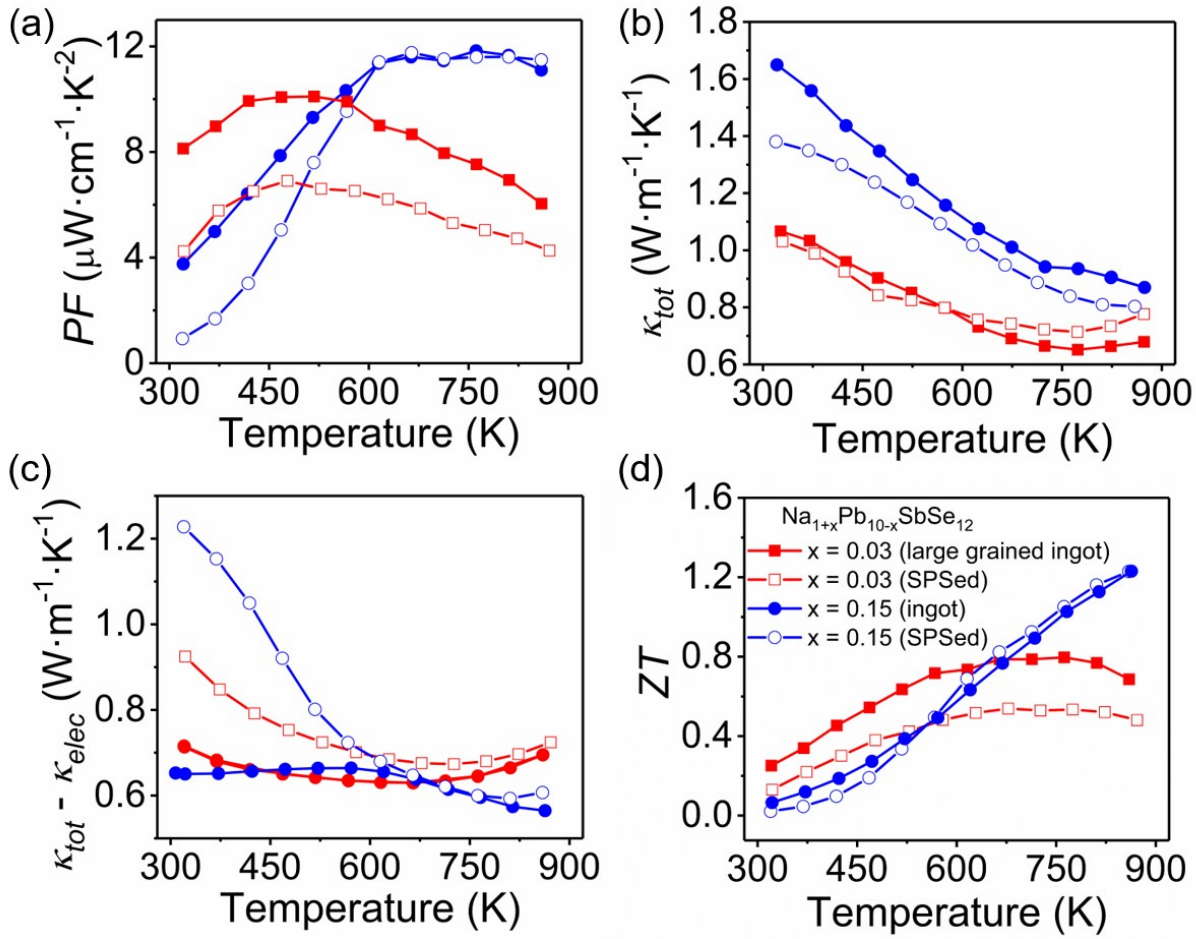

Figure S12: (a) Power factors, (b) total thermal conductivities, (c) estimated lattice thermal conductivity, and (d) *ZT* for as–cast ingots (large grained samples) and SPS–processed (small grains) $Na_{1+x}Pb_{10-x}SbSe_{12}$. The electronic properties for these samples are discussed in Figure 2 of the main text. Because of the improved charge carrier mobility, the power factors are enhanced in the large grained samples. The figures of merit for the x = 0.03 (lightly doped) sample is significantly improved for the larger grained sample. The enhancement is more modest in the large-grained forms of the more heavily doped x = 0.15 samples. More detail on the lattice thermal conductivities is given in the discussion of Figure S13.

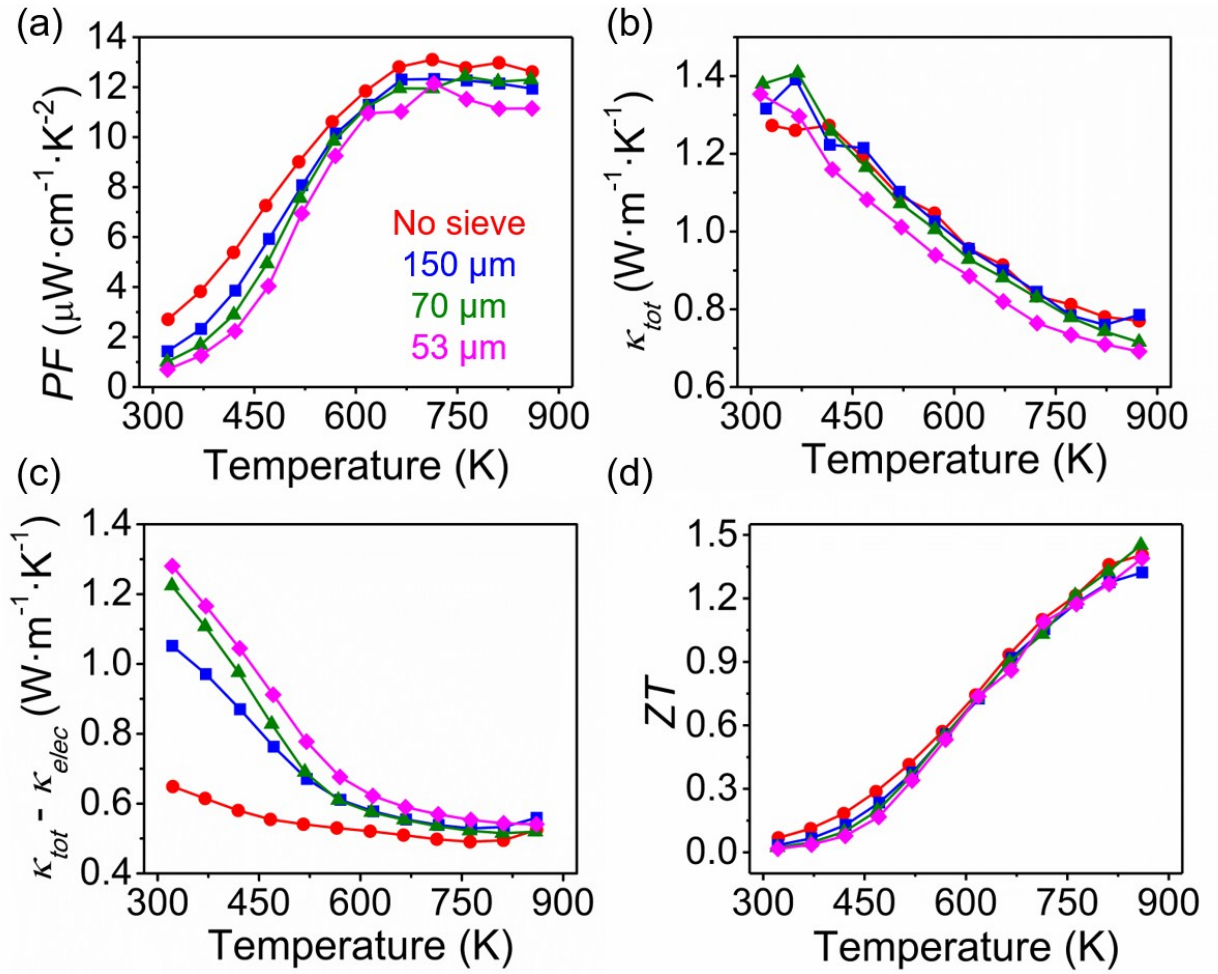

Figure S13: (a) Power factors, (b) total thermal conductivities, (c) estimated lattice thermal conductivity, and (d) *ZT* for samples with nominal composition of $Na_{1.10}Pb_{9.90}Sb_{0.90}Se_{12}$. The samples were prepared by SPS-sintering powders that were first passed through sieves with different mesh sizes. The electronic properties for these samples are discussed in Figure S7. Because of the improved charge carrier mobility, the power factors are increasingly enhanced as the grain size increases. The figures of merit are likewise modestly enhanced at low temperature as the grain size is raised.

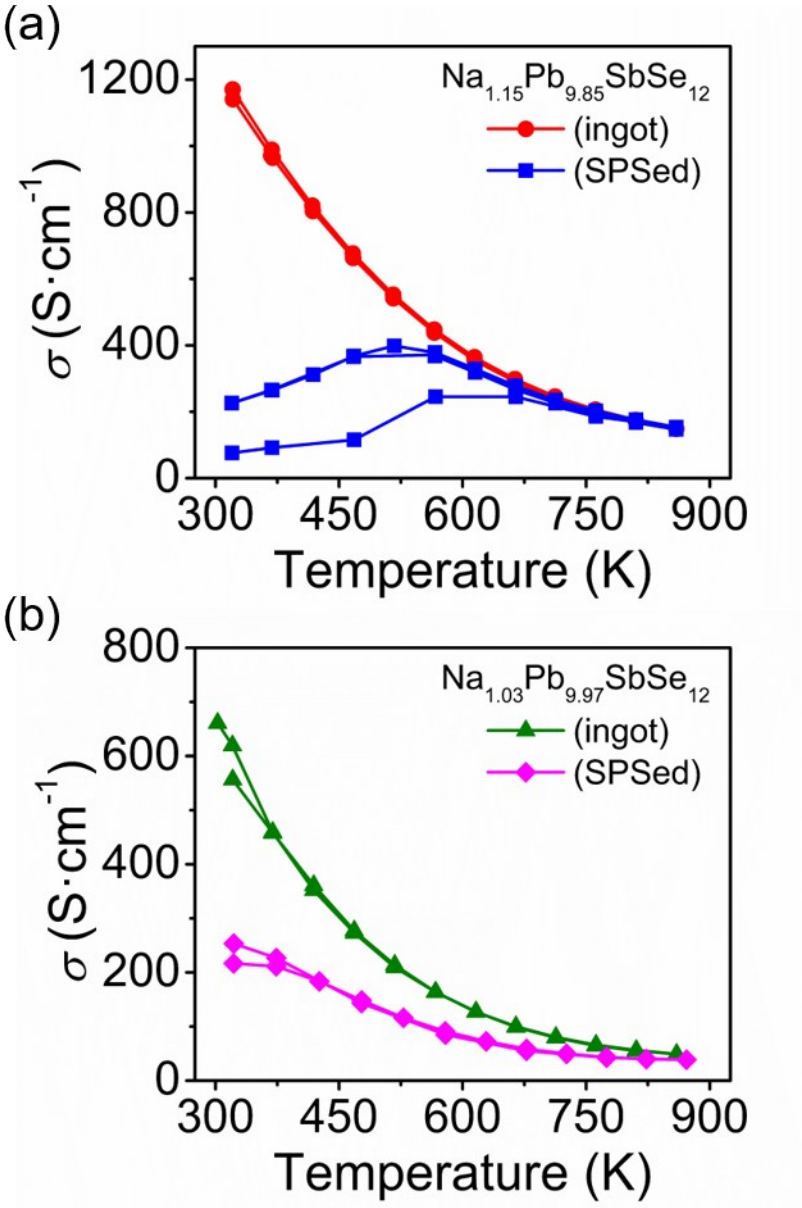

Figure S14: Variable-temperature electrical conductivity measured for as-cast ingots and SPS processed samples of $Na_{1+x}Pb_{10-x}SbSe_{12}$ (a) x = 0.15, and (b) x = 0.03. Both heating and cooling profiles are shown. The cooling profiles for each are shown in Figure 2 of the main text. The data for the x = 0.15 SPS processed sample shows significant hysteresis which stabilizes after the initial heating step. Hysteresis of this type, which stabilized after heating to ~ 900 K, was regularly observed in the samples with strong GB scattering. Interestingly, such hysteresis is not seen in the large grained ingot samples or the lightly doped materials, both of which have negligible GB resistance. At this point we do not fully understand the hysteretic behavior of the heavily doped small grained samples, but this could feasibly due to grain coarsening during the initial heating with negligible changes upon further thermal cycling.

Table S1: Room temperature Hall coefficients and Hall charge carrier densities for $NaPb_mSbSe_{m+2}$ m = 6, 20 and $NaPb_mSbSe_{m+2}$ m = 20. Nominal compositions are $Na_{1.10}Pb_{5.90}Sb_xSe_8$ and $Na_{1+x}Pb_{20-x}SbSe_{22}$, and $Na_{1+x}Pb_{20-x}SbS_{22}$.

Nominal Composition	R_H (10^{-2} $cm^{-3}C^{-1}$)	n_H (10^{19} cm^{-3})
$Na_{1.10}Pb_{5.90}Sb_{0.90}Se_8$	6.08	10.27
$Na_{1.05}Pb_{19.95}SbSe_{22}$	24.22	2.58
$Na_{1.10}Pb_{19.90}SbSe_{22}$	6.43	9.70
$Na_{1.15}Pb_{19.85}SbSe_{22}$	8.70	7.17
$Na_{1.20}Pb_{19.80}SbSe_{22}$	4.40	14.2
$Na_{1.25}Pb_{19.75}SbSe_{22}$	4.05	15.4
$Na_{1.30}Pb_{19.70}SbSe_{22}$	3.61	17.3
$Na_{1.10}Pb_{19.90}SbS_{22}$	11.9	5.25
$Na_{1.15}Pb_{19.85}SbS_{22}$	4.21	14.8

References:

1. J. Y. W. Seto, *J. Appl. Phys.*, 1975, **46**, 5247-5254.
2. T. J. Slade, T. P. Bailey, J. A. Grovogui, X. Hua, X. Zhang, J. J. Kuo, I. Hadar, G. J. Snyder, C. Wolverton, V. P. Dravid, C. Uher and M. G. Kanatzidis, *Advanced Energy Materials*, 2019, **9**, 1901377.
3. J. J. Kuo, M. Wood, T. J. Slade, M. G. Kanatzidis and G. J. Snyder, *Energy & Environmental Science*, 2020, DOI: 10.1039/C9EE03921J.